Element-local level set method for three-dimensional dynamic crack growth

Qinglin Duan[‡], Jeong-Hoon Song[‡], Thomas Menouillard[‡] and Ted Belytschko[*,†,§]

Department of Mechanical Engineering, Northwestern University, Evanston, IL 60208-3111, U.S.A.

SUMMARY

An approximate level set method for three-dimensional crack propagation is presented. In this method, the discontinuity surface in each cracked element is defined by element-local level sets (ELLSs). The local level sets are generated by a fitting procedure that meets the fracture directionality and its continuity with the adjacent element crack surfaces in a least-square sense. A simple iterative procedure is introduced to improve the consistency of the generated element crack surface with those of the adjacent cracked elements. The discrete discontinuity is treated by the phantom node method which is a simplified version of the extended finite element method (XFEM). The ELLS method and the phantom node technology are combined for the solution of dynamic fracture problems. Numerical examples for three-dimensional dynamic crack propagation are provided to demonstrate the effectiveness and robustness of the proposed method. Copyright © 2009 John Wiley & Sons, Ltd.

1. INTRODUCTION

We present a new level set update method for three-dimensional crack propagation. In this method, the level sets are defined locally for each element and as the crack propagates, the local signed distance function is generated for each new cracked element by a procedure that satisfies the fracture directionality and its continuity with the adjacent element crack surfaces in a least-square sense. Therefore, in contrast to conventional level set methods, the method does not require a

---

velocity of the crack front and is applicable to a large variety of failure criteria, such as material instability criteria, various phenomenological criteria and strain criteria. Consequently, it facilitates the application of such fracture criteria to both fracture dynamics and mechanics.

Prediction of material failure by fracture is of major concern in many engineering problems. In the past decades, several types of computational methods have been developed to model fracture. The embedded discontinuity methods [1–3] treat the crack as a band of high strain or by an equivalent incompatible discontinuity in the element; see [4] for a comprehensive study of these methods. The inter-element fracture methods of Xu and Needleman [5] and Ortiz and Pandolfi [6] simulate the crack as inter-element discontinuities with cohesive forces. These methods are simple and robust, but the direction of the crack is limited to the element edges or interfaces, i.e. the crack paths are limited to specified directions. This drawback impairs the capability of these methods to accurately reproduce crack paths.

The extended finite element method (XFEM) permits arbitrary discontinuities to be modeled by finite elements without remeshing via discontinuous partitions of unity. Belytschko and Black [7] used the discontinuous near tip field with partitions of unity enrichments to model the entire crack for elastostatic problems. Moës et al. [8] and Dolbow et al. [9] introduced step function enrichments for the finite element basis that can model discontinuities independent of the mesh topology and called the method XFEM. In Belytschko et al. [10] the approach was generalized to arbitrary discontinuities including discontinuities in derivatives and tangential components of displacements.

Applications of XFEM to fracture dynamics have been reported by Belytschko et al. [11], Réthoré et al. [12], Song et al. [13], and Menouillard et al. [14]. Song et al. [13] used a rearrangement of the extended finite element basis and the nodal degrees of freedom, so that the discontinuity can be described by superposed elements and phantom nodes; this form corresponds to the concept proposed by Hansbo and Hansbo [15].

The conventional level set method [16] was combined with XFEM for crack propagation analysis by Stolarska et al. [17] and Belytschko et al. [10] for 2D and Moës et al. [18] and Gravouil et al. [19] for 3D. In this method, the discontinuity is implicitly defined by two signed distance functions: one defines the crack surface and its intersection with the second defines the crack front. The merit of this method is that the resulting crack surface and crack front are smooth. However, the conventional level set method requires a knowledge of the crack front velocity. When fracture is driven by a stress- or strain-based criteria, such as material instability criteria or phenomenological criteria, the velocity is not well defined and usually cannot be easily computed.

Methods that do not use conventional level sets for three-dimensional crack propagation were introduced by Areias and Belytschko [20] and Gasser and Holzapfel [21, 22]. They sought to satisfy the continuity of the crack surface and the fracture direction criterion approximately. These two conditions can easily be met for two-dimensional problems, because the crack front in 2D is just a point, i.e. the crack tip. However, for three-dimensional problems the crack front is a spatial curve, and it is generally not possible to meet continuity of the crack surface and a fracture directionality criterion simultaneously.

Areias and Belytschko [20] addressed this difficulty by adjusting the crack plane normal to satisfy continuity. However, this adjustment may lead to significant deviations of the propagation direction from the direction determined by the fracture criterion. Except for this drawback, their method produces relatively smooth discontinuity surfaces and is computationally efficient because the algorithm is restricted to the element level. Gasser and Holzapfel [21, 22] proposed an alternative strategy that is based on non-local averaging. The set of intersection points of the adjacent element

discontinuities with the element edges is used to fit the crack surface for the element of interest. This method appears to work well for curved and even kinked crack surfaces, but due to the nonlocal averaging, inter-element jumps maybe occur in the overall crack surface representation and the flexibility of the method is impaired. Furthermore, the fracture criterion is not included in their averaging process which can lead to a violation of the fracture directionality. These two methods are studied and compared by Jäger *et al.* [23].

Pereira *et al.* [24] have used triangular facet representations of cracks in three dimensions in conjunction with the generalized finite element method of Duarte *et al.* [25, 26].

In this paper, we develop a method for modeling dynamic fracture in three dimensions by combining a variant of XFEM with an element-local level set (ELLS) method. The mechanical description of the crack is based on the phantom node method [13], which was originated by Hansbo and Hansbo [15]; the basis functions for this method are identical to XFEM for the fully cracked elements considered here, but the implementation is somewhat simpler for dynamics. The method is implemented with an explicit time-integration algorithm with stabilized one-point quadrature elements [27, 28].

The key contribution of this paper is the ELLS method which describes the crack surface. This surface is developed element-wise so that it satisfies continuity of the crack surface between elements and the fracture direction criterion in a least-square sense. An approximation to a smooth surface is required because it is usually impossible to find a surface in an element that is continuous with that of the adjacent cracked elements and is also in the direction predicted by a fracture criterion. The description herein is limited to the propagation of a single crack, but extension to multiple cracks should not be difficult.

This paper is organized as follows. Section 2 describes the governing equations and the cohesive model we will use. Then we introduce the ELLS description for crack surface and the least-square fitting procedure to determine the crack growth in Section 3. The displacement field of the phantom node method for modeling elements with discontinuities is given in Section 4. The weak form and the discretized equations are summarized in Section 5. Numerical studies are described in Section 6. Concluding remarks are provided in Section 7.

2. GOVERNING EQUATIONS AND THE COHESIVE MODEL

We consider a three-dimensional dynamic problem. As shown in Figure 1, the motion is described by $\mathbf{x} = \boldsymbol{\phi}(\mathbf{X}, t)$ which maps the initial configuration Ω_0 to the current configuration Ω. $\mathbf{X}$ and $\mathbf{x}$ denote material and spatial coordinates, respectively. The crack surface and its front in initial domain are denoted by Γ_c^0 and ξ_c^0, respectively. Their images in current domain are Γ_c and ξ_c, respectively.

The strong form of the linear momentum equation in a total Lagrangian description is

$$\frac{\partial P_{ji}}{\partial X_j} + \rho_0 b_i - \rho_0 \ddot{u}_i = 0 \quad \text{in } \Omega_0 \backslash \Gamma_c^0 \tag{1}$$

where $\mathbf{P}$ is the nominal stress tensor, ρ_0 the initial mass density, $\mathbf{u}$ the displacement and $\mathbf{b}$ the body force per unit mass. The boundary and interior conditions are

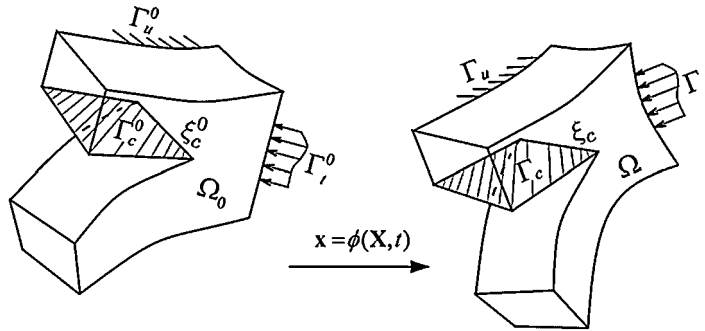$$n_j^0 P_{ji} = \bar{t}_i^0 \quad \text{on } \Gamma_t^0 \tag{2}$$

Figure 1. A three-dimensional body with a discontinuity and its representation in the
initial and the current domains.

$$u_i = \bar{u}_i \quad \text{on } \Gamma_u^0 \tag{3}$$

$$n_j^0 P_{ji}^- = -n_j^0 P_{ji}^+ = \tau_i^{0c}([[u_i]]) \quad \text{on } \Gamma_c^0 \tag{4}$$

where $\mathbf{n}^0$ is the normal to the indicated boundary, $\boldsymbol{\tau}^{0c}$ the cohesive traction across the crack, $\bar{\mathbf{t}}^0$ the applied traction on the Neumann boundary Γ_t^0 and $\bar{\mathbf{u}}$ the applied displacement on the Dirichlet boundary Γ_u^0. We have $\Gamma_u^0 \cup \Gamma_t^0 = \Gamma^0$ and $\Gamma_u^0 \cap \Gamma_t^0 = \emptyset$. Plus and minus superscripts refer to the two sides of the discontinuity. Indicial notation is used for any lower-case indices and repeated subscripts imply summations.

To illustrate the method, we will use a Kirchhoff material, which is a straightforward generalization of linear elasticity to large deformations. The constitutive relation for an isotropic Kirchhoff material may be written as

$$S_{ij} = C_{ijkl} E_{kl} \tag{5}$$

where S_{ij} is the second Piola–Kirchhoff (PK2) stress tensor, E_{kl} the Green (Green–Lagrange) strain tensor which is defined as

$$E_{ij} = \frac{1}{2}\left(\frac{\partial u_i}{\partial X_j} + \frac{\partial u_j}{\partial X_i} + \frac{\partial u_k}{\partial X_i}\frac{\partial u_k}{\partial X_j} \right) \tag{6}$$

C_{ijkl} in Equation (5) is the fourth-order tensor of elastic moduli which is given by

$$C_{ijkl} = \lambda \delta_{ij}\delta_{kl} + \mu(\delta_{ik}\delta_{jl} + \delta_{il}\delta_{jk}) \tag{7}$$

where λ and μ are the Lamé constants which can be expressed in terms of Young's modulus E and the Poisson ratio v by

$$\lambda = \frac{vE}{(1+v)(1-2v)}, \quad \mu = \frac{E}{2(1+v)} \tag{8}$$

We use a strain fracture criterion with a cohesive law. In the strain criterion, the material is considered to fracture when

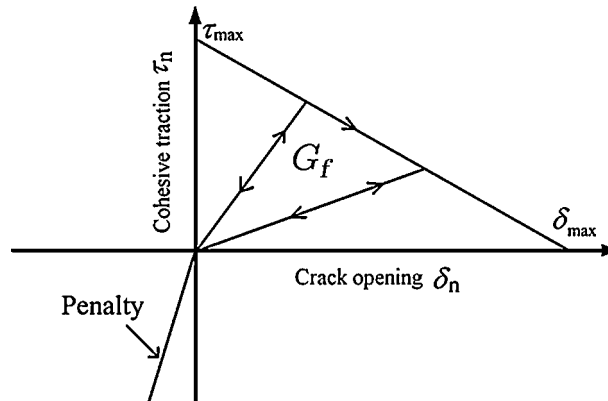$$\max\{\lambda_i\} > \varepsilon_f \tag{9}$$

Figure 2. Schematic of the linear cohesive law: the area under curve is the fracture energy G_f.

where λ_i are the eigenvalues of the Green–Lagrange strain $\mathbf{E}$ and ε_f is the failure strain. The normal of the failure surface $\mathbf{N}^e$ is assumed to be coincident with the eigenvector associated with $\max\{\lambda_i\}$. However, to avoid spurious crack path oscillations, especially for dynamic simulations, a non-local smoothed strain is used to determine the normal $\mathbf{N}^e$ in element e instead of the local strain. We first compute the eigenvalues λ_i^e of the average strain and let

$$\mathbf{N}^e = \mathbf{Z}_i \tag{10}$$

where $\mathbf{Z}_i$ is the eigenvector corresponding to the maximum eigenvalue λ_i^e. The average strain was computed over a domain with a radius of $3h$–$5h$, where h is the element size. We can also use the polarization direction as given by the material stability criterion as in [11]. Note that a single normal is associated with the failure surface since one-point quadrature elements are used; in the actual trilinear surface, the normal varies in the element.

A cohesive crack model [29–34] is assumed, i.e. a surface traction is applied along the crack surface. The cohesive traction is determined by a cohesive law which relates the traction to the jump in displacement across the discontinuity surface. In this study, the linear cohesive law shown in Figure 2 is employed so that the energy dissipated due to the crack propagation matches the critical fracture energy, i.e. the critical crack opening $\delta_{\max}$ is calculated by

$$\delta_{\max} = \frac{2G_f}{\tau_{\max}} \tag{11}$$

where G_f is the fracture energy, $\tau_{\max}$ is set to the traction across the crack at the time of fracture to ensure the time continuity for the cohesive crack model [35]. Note that a penalty force is added to treat the crack surface overlap. In this work, we consider only the normal component of the cohesive traction.

3. ELEMENT-LOCAL LEVEL SET (ELLS) DESCRIPTION AND ITS GENERATION FOR CRACK GROWTH

This section describes the procedure for generating the ELLS. As indicated in the Introduction, the objective is to generate a surface that meets continuity with the existing crack and the fracture

directionality criterion as close as possible; in this case, we adopt this to mean in a least-square sense.

In this procedure, element is either cracked or uncracked; partially cracked elements are not considered. We consider a crack surface whose image in the reference configuration is Γ_c^0 with a crack front ξ_c^0. Let S_Γ be the set of cracked elements. The crack surface is approximated by element crack surfaces Γ_c^{e0}, so that the approximate crack surface Γ_c^{0h} is given by

$$\Gamma_c^{0h} = \bigcup_{e \in S_\Gamma} \Gamma_c^{e0} \tag{12}$$

The resulting surface is generally not a continuous surface. The subset of elements in S_Γ that are adjacent to uncracked elements are denoted by S_ξ.

3.1. Element-local level set (ELLS) description for element crack surface Γ_c^{e0}

The crack surface in element e is implicitly defined by the element-local signed distance function $f^e(\mathbf{X})$ so that $f^e(\mathbf{X}) = 0$ gives the element discontinuity surface Γ_c^{e0}. This implicit definition is described in terms of the nodal shape functions $\Phi_I(\mathbf{X})$ of element e by

$$\sum_{I \in e} \Phi_I(\mathbf{X}) f_I^e = 0 \tag{13}$$

where f_I^e are the nodal values of the element-local signed distance function $f^e(\mathbf{X})$. The normal of the element crack surface is

$$\mathbf{n}^e = \mathbf{n}(f_I^e) = \frac{\partial f^e(\mathbf{X})}{\partial \mathbf{X}} = \sum_{I \in e} \frac{\partial \Phi_I(\mathbf{X})}{\partial \mathbf{X}} f_I^e \tag{14}$$

Note that for hexahedral elements the element crack surface defined by Equation (13) is generally not a plane. However, due to the nature of bilinear interpolation, it will not deviate from a plane too much.

3.2. Generation of ELLSs for crack growth

Let S_p be the set of elements that are intact (uncracked) and share the crack front with elements in S_ξ. Initially, the ELLSs in elements in S_p are not given. As the crack front propagates, some of these elements will crack and the ELLSs for them must be generated to define the crack surfaces in these elements.

Unlike in two dimensions, even for a single crack in 3D, there are several elements along the crack front and several of these will be cracked in a given time step. Because we use element-wise cracking, elements crack one by one. Here, we use the largest eigenvalue $\max\{\lambda_i\}$ of the Green–Lagrange strain $\mathbf{E}$ as an indicator to set up the sequence, i.e. the element with the largest value of $\max\{\lambda_i\}$ will be first cracked.

Let $\mathbf{N}^e$ be the normal to the crack in element e as given by the fracture criterion and $\mathbf{n}(f_I^e)$ the normal in terms of the ELLSs of element e as given by Equation (14). The nodal values of the ELLSs for element e are determined by minimizing $J(f_I^e)$ which is given by

$$J(f_I^e) = \int_{\Omega_0^e} \|\mathbf{N}^e - \mathbf{n}(f_I^e)\|^2 \, d\Omega_0^e + \sum_{I \in S_e^0} \int_{\Omega_0^e} w_I \left(\frac{f_I^e - \bar{f}_I}{h_e} \right)^2 d\Omega_0^e \tag{15}$$

where S_e^0 is the set of nodes of element e which are shared with adjacent cracked elements. w_I is a weight for node I which controls the jump of the crack surface at node I. h_e is the characteristic size of element e which is set to be equal to the minimum size of the element edges. $\bar{f}_I$ is the average of the ELLS functions for all elements other than e that share node I, that is

$$\bar{f}_I = \frac{1}{n_I} \sum_{k=1}^{n_I} f_I^k \tag{16}$$

where n_I is the number of the adjacent cracked elements which share node I with the current element e. Note that if the weight w_I is small, moderate inter-element discontinuities will occur in the resulting crack surface. However, it satisfies the fracture directionality better. On the contrary, if w_I is large, the discontinuities in the resulting crack surface are smaller but it impairs the satisfaction of the fracture directionality. According to our experience, $w_I = 1$ is an appropriate value to balance the continuity and fracture directionality. We will show this in our numerical results.

Substituting Equation (14) into Equation (15), the minimization yields the following equation:

$$(\mathbf{K} + \mathbf{W}) \mathbf{f}^e = \mathbf{p} + \bar{\mathbf{p}} \tag{17}$$

where

$$K_{IJ} = \int_{\Omega_0^e} \frac{\partial \Phi_I(\mathbf{X})}{\partial \mathbf{X}} \cdot \frac{\partial \Phi_J(\mathbf{X})}{\partial \mathbf{X}} \, \mathrm{d}\Omega_0^e \tag{18}$$

$$\mathbf{W} = \mathrm{diag}\{W_1, W_2, \ldots, W_8\} \quad W_I = \begin{cases} \int_{\Omega_0^e} \frac{w_I}{h_e^2} \, \mathrm{d}\Omega_0^e & \text{if } I \in S_e^0 \\ 0 & \text{otherwise} \end{cases} \tag{19}$$

$$\mathbf{f}^e = \{f_1^e, f_2^e, \ldots, f_8^e\} \tag{20}$$

$$p_I = \int_{\Omega_0^e} \frac{\partial \Phi_I(\mathbf{X})}{\partial \mathbf{X}} \cdot \mathbf{N}^e \, \mathrm{d}\Omega_0^e \tag{21}$$

$$\bar{p}_I = \begin{cases} \int_{\Omega_0^e} \frac{w_I \bar{f}_I}{h_e^2} \, \mathrm{d}\Omega_0^e & \text{if } I \in S_e^0 \\ 0 & \text{otherwise} \end{cases} \tag{22}$$

$2 \times 2 \times 2$ Gauss quadrature is used to evaluate the integrals in the above equations.

We now further explain our reasons for choosing this method. As pointed out before, two conditions should be met in each element by the crack surface. One is that the generated crack surface should be perpendicular to the normal determined by the fracture criterion, i.e. $\mathbf{N}^e$ in Equation (10); the other is that the generated crack surface should pass through the crack front, i.e. be continuous with the existing crack. The difficulty is that these two conditions generally can not both be met. For example, consider the situation shown in Figure 3 where the crack is planar. Any surface through crack fronts $\mathbf{A}$ and $\mathbf{B}$ has normal $\mathbf{A} \times \mathbf{B}$. If $\mathbf{N}^e \neq \mathbf{A} \times \mathbf{B}$ then the new crack surface will need to be discontinuous with $\mathbf{A}$ and $\mathbf{B}$.

Even when only a single edge of the crack is adjacent to an element that cracks next, satisfying continuity and the fracture directionality criterion may not be possible. An example is shown in
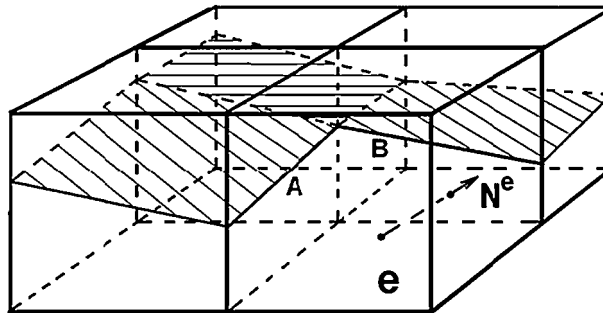
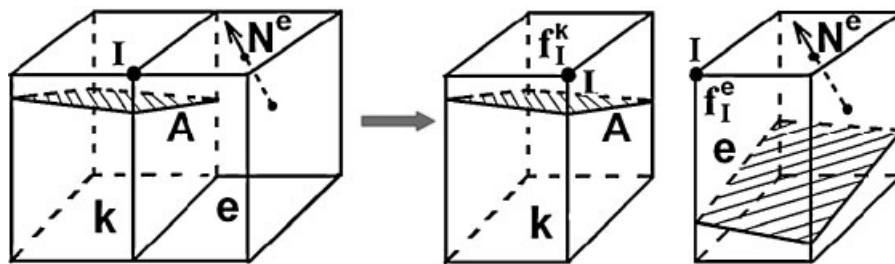Figure 3. Inconsistency of crack fronts and the fracture directionality.

Figure 4. Element-local level sets for crack propagation: node I has different local level set values f_I^e and f_I^k for two adjacent elements.

Figure 4: the crack is propagating from element k to element e and element e is the element to be cracked. Generally, the normal $\mathbf{N}^e$ is not perpendicular to the crack front $\mathbf{A}$. In this case, we cannot generate an element crack surface which can pass through $\mathbf{A}$ and be perpendicular to $\mathbf{N}^e$ at the same time.

The fundamental idea of our method is to satisfy these two conditions approximately instead of exactly, i.e. in a least-square sense as shown in Equation (15). In fact, the first and second terms on the right-hand side of Equation (15), respectively, correspond to the first and second conditions mentioned above. Owing to this approximation, the resulting crack surface, generally, is not continuous with the crack front, i.e. $f_I^e \neq f_I^k$ in Figure 4.

If an edge of element e is already cut by the crack surface, the crack surface of element e is required to cut this edge. This corresponds to the following condition:

$$\bar{f}_I \cdot f_I^e > 0 \quad \forall I \tag{23}$$

However, f_I^e as determined by Equation (17) cannot ensure that this condition is satisfied. Therefore, a simple iteration process is introduced: when $\bar{f}_I \cdot f_I^e < 0$, we increase the corresponding weight w_I (generally by doubling it), reconstruct Equation (17) and solve it to get a new f_I^e until Equation (23) is satisfied.

4. PHANTOM NODES FOR 3D CRACKED ELEMENTS

In conventional XFEM, the displacement field for a completely cracked element e is of the following form:

$$\mathbf{u}(\mathbf{X}, t) = \sum_{I=1}^{n_e} \Phi_I(\mathbf{X})\{\mathbf{u}_I(t) + \mathbf{q}_I[H(f^e(\mathbf{X})) - H(f^e(\mathbf{X}_I))]\} \tag{24}$$

where n_e is the number of nodes per element, $\mathbf{u}_I$ and $\mathbf{q}_I$ are, respectively, the nodal values and additional degrees of freedom associated with the enrichment for the discontinuity. $H(x)$ is the Heaviside step function given by

$$H(x) = \begin{cases} 1 & \text{if } x > 0 \\ 0 & \text{if } x \leqslant 0 \end{cases} \tag{25}$$

In [13], Song *et al.* have already shown that by a rearrangement of the extended finite element basis and the nodal degrees of freedom, the discontinuity can be described by superposed elements and phantom nodes. Thus, the displacement field of Equation (24) can be written as

$$\mathbf{u}(\mathbf{X}, t) = \sum_{I \in S_1} \underbrace{\mathbf{u}_I^1(t)\Phi_I(\mathbf{X})}_{\mathbf{u}^1(\mathbf{X}, t)} H(f^e(\mathbf{X})) + \sum_{I \in S_2} \underbrace{\mathbf{u}_I^2(t)\Phi_I(\mathbf{X})}_{\mathbf{u}^2(\mathbf{X}, t)} H(-f^e(\mathbf{X})) \tag{26}$$

where S_1 and S_2 are the index sets of the nodes of superposed element 1 and 2, respectively. $\mathbf{u}_I^1$ and $\mathbf{u}_I^2$ are the nodal degrees of freedom of the superposed element 1 and 2, respectively, and are defined as

$$\mathbf{u}_I^1 = \begin{cases} \mathbf{u}_I & \text{if } f^e(\mathbf{X}_I) > 0 \\ \mathbf{u}_I + \mathbf{q}_I & \text{if } f^e(\mathbf{X}_I) < 0 \end{cases} \tag{27}$$

$$\mathbf{u}_I^2 = \begin{cases} \mathbf{u}_I - \mathbf{q}_I & \text{if } f^e(\mathbf{X}_I) > 0 \\ \mathbf{u}_I & \text{if } f^e(\mathbf{X}_I) < 0 \end{cases} \tag{28}$$

As shown in Figure 5, each element contains both the original real nodes and the phantom nodes and $\mathbf{u}^1(\mathbf{X}, t)$ holds for $f^e(\mathbf{X}) > 0$ and the other $\mathbf{u}^2(\mathbf{X}, t)$ holds for $f^e(\mathbf{X}) < 0$. Such recasting effectively simplifies the implementation of XFEM, as the element force of the superposed elements can be calculated in the same way as in the conventional finite element method. This will be further classified in the next section.

5. WEAK FORM AND DISCRETIZED EQUATIONS

The discrete equations are constructed by the standard Galerkin procedures. The admissible space for the displacement fields is defined as follows:

$$\mathscr{U} = \{\mathbf{u}(\mathbf{X}, t) | \mathbf{u}(\mathbf{X}, t) \in C^0, \mathbf{u}(\mathbf{X}, t) = \bar{\mathbf{u}}(t) \text{ on } \Gamma_u^0, \mathbf{u} \text{ discontinuous on } \Gamma_c^0\}$$

$$\mathscr{U}_0 = \{\delta\mathbf{u}(\mathbf{X}, t) | \delta\mathbf{u}(\mathbf{X}, t) \in C^0, \delta\mathbf{u}(\mathbf{X}, t) = 0 \text{ on } \Gamma_u^0, \delta\mathbf{u} \text{ discontinuous on } \Gamma_c^0\}$$
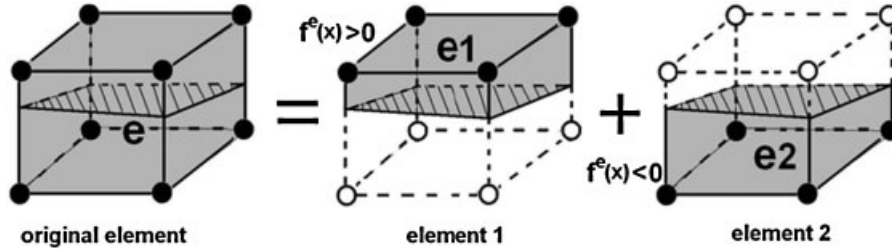
Figure 5. The decomposition of a cracked element into two elements: solid and hollow circles denote the original nodes and the added *phantom* nodes, respectively.

The weak form of the momentum equation is given by: for $\mathbf{u}(\mathbf{X}, t) \in \mathcal{U}$

$$\delta W^{\mathrm{kin}} = \delta W^{\mathrm{ext}} - \delta W^{\mathrm{int}} - \delta W^{\mathrm{coh}} \quad \forall \delta\mathbf{u}(\mathbf{X}) \in \mathcal{U}_0 \tag{29}$$

where δW^{int} is the virtual internal work, δW^{ext} the virtual external work performed by applied loads, δW^{kin} the virtual kinetic work performed by inertia and δW^{coh} the virtual work performed by the cohesive traction on the crack surface Γ_c. They are defined by

$$\delta W^{\mathrm{kin}} = \int_{\Omega_0 \setminus \Gamma_c^0} \delta\mathbf{u} \cdot \rho_0 \ddot{\mathbf{u}} \, \mathrm{d}\Omega_0 \tag{30}$$

$$\delta W^{\mathrm{int}} = \int_{\Omega_0 \setminus \Gamma_c^0} \frac{\partial \delta\mathbf{u}}{\partial \mathbf{X}} : \mathbf{P} \, \mathrm{d}\Omega_0 \tag{31}$$

$$\delta W^{\mathrm{ext}} = \int_{\Omega_0 \setminus \Gamma_c^0} \delta\mathbf{u} \cdot \rho_0 \mathbf{b} \, \mathrm{d}\Omega_0 + \int_{\Gamma_t^0} \delta\mathbf{u} \cdot \bar{\mathbf{t}}^0 \, \mathrm{d}\Gamma_t^0 \tag{32}$$

$$\delta W^{\mathrm{coh}} = \int_{\Gamma_c} \delta[[\mathbf{u}]] \cdot \boldsymbol{\tau}^c \, \mathrm{d}\Gamma_c \tag{33}$$

where $\boldsymbol{\tau}^c$ is the cohesive traction applied on the discontinuity surface. Note that the cohesive work is evaluated in current domain as shown in Equation (33).

By performing the spatial discretization of Equation (29), the discrete momentum equation is

$$\mathbf{f}^{\mathrm{kin}} = \mathbf{f}^{\mathrm{ext}} - \mathbf{f}^{\mathrm{int}} - \mathbf{f}^{\mathrm{coh}} \tag{34}$$

where $\mathbf{f}^{\mathrm{int}}$, $\mathbf{f}^{\mathrm{ext}}$ and $\mathbf{f}^{\mathrm{coh}}$ are the nodal internal force, external force and cohesive force, respectively. They are assembled from each element nodal forces; please note that bold $\mathbf{f}$ are nodal forces, f the level set. For a cracked element e, its two superposed elements nodal forces can be, respectively, written as

$$\mathbf{f}_{ei}^{\mathrm{kin}} = \int_{\Omega_0^e} \rho_0 \boldsymbol{\Phi}^{\mathrm{T}} \boldsymbol{\Phi} H((-1)^{i+1} f^e(\mathbf{X})) \, \mathrm{d}\Omega_0^e \ddot{\mathbf{u}}_e \tag{35}$$

$$\mathbf{f}_{ei}^{\mathrm{int}} = \int_{\Omega_0^e} \mathbf{B}_0^{\mathrm{T}} \mathbf{P}_e H((-1)^{i+1} f^e(\mathbf{X})) \, \mathrm{d}\Omega_0^e \tag{36}$$

$$\mathbf{f}_{ei}^{\text{ext}} = \int_{\Omega_0^e} \rho_0 \mathbf{\Phi}^{\text{T}} \mathbf{b} H((-1)^{i+1} f^e(\mathbf{X})) \, \mathrm{d}\Omega_0^e + \int_{\Gamma_t^{e0}} \mathbf{\Phi}^{\text{T}} \bar{\mathbf{t}}^0 H((-1)^{i+1} f^e(\mathbf{X})) \, \mathrm{d}\Gamma_t^{e0} \tag{37}$$

$$\mathbf{f}_{ei}^{\text{coh}} = (-1)^i \int_{\Gamma_c^e} \mathbf{\Phi}^{\text{T}} \tau^c \mathbf{n}^e \, \mathrm{d}\Gamma_c^e \tag{38}$$

where $f^e(\mathbf{X})$ is the ELLS function for element e, i is 1 and 2 denote the two superposed elements as shown in Figure 5 and $\mathbf{B}_0$ is the discrete strain–displacement operator with respect to the reference coordinates, see Belytschko *et al.* [36]. Note that the nodal forces of element e are the sum of the nodal forces of the two superposed elements, i.e.

$$\mathbf{f}_e = \mathbf{f}_{e1} + \mathbf{f}_{e2} \tag{39}$$

where $\mathbf{f}_e$ is the element force vector of cracked element and $\mathbf{f}_{e1}$ and $\mathbf{f}_{e2}$ are the force vectors of the superposed elements. By expanding Equations (35)–(38), $\mathbf{f}_{e1}$ and $\mathbf{f}_{e2}$ can be written as

$$\mathbf{f}_{(e1/e2)}^{\text{kin}} = \frac{V_{(e1/e2)}}{V_0} \int_{\Omega_0^e} \rho_0 \mathbf{\Phi}^{\text{T}} \mathbf{\Phi} \, \mathrm{d}\Omega_0^e \ddot{\mathbf{u}}_{(e1/e2)} \tag{40}$$

$$\mathbf{f}_{(e1/e2)}^{\text{int}} = \frac{V_{(e1/e2)}}{V_0} \int_{\Omega_0^e} \{\mathbf{B}_0^{\text{T}} \mathbf{P}_{(e1/e2)} + \mathbf{f}_{(e1/e2)}^{\text{stab}}\} \, \mathrm{d}\Omega_0^e \tag{41}$$

$$\mathbf{f}_{e1}^{\text{ext}} = \frac{V_{e1}}{V_0} \int_{\Omega_0^e} \rho_0 \mathbf{\Phi}^{\text{T}} \mathbf{b} \, \mathrm{d}\Omega_0^e + \int_{\Gamma_t^{e0}} H(f^e(\mathbf{X})) \mathbf{\Phi}^{\text{T}} \bar{\mathbf{t}}^0 \, \mathrm{d}\Gamma_t^{e0} \tag{42}$$

$$\mathbf{f}_{e2}^{\text{ext}} = \frac{V_{e2}}{V_0} \int_{\Omega_0^e} \rho_0 \mathbf{\Phi}^{\text{T}} \mathbf{b} \, \mathrm{d}\Omega_0^e + \int_{\Gamma_t^{e0}} H(-f^e(\mathbf{X})) \mathbf{\Phi}^{\text{T}} \bar{\mathbf{t}}^0 \, \mathrm{d}\Gamma_t^{e0} \tag{43}$$

$$\mathbf{f}_{e1}^{\text{coh}} = - \int_{\Gamma_c^e} \mathbf{\Phi}^{\text{T}} \tau^c \mathbf{n}^e \, \mathrm{d}\Gamma_c^e \tag{44}$$

$$\mathbf{f}_{e2}^{\text{coh}} = \int_{\Gamma_c^e} \mathbf{\Phi}^{\text{T}} \tau^c \mathbf{n}^e \, \mathrm{d}\Gamma_c^e \tag{45}$$

where V_0 is the total volume of the uncracked element and V_{e1} and V_{e2} are the activated volumes (gray region in Figure 5) of the corresponding superposed elements which consist of regular and phantom nodes. $\mathbf{f}^{\text{stab}}$ in Equation (41) is a stabilization force to control the hourglass modes since we adopt the one-point integration scheme to evaluate the element internal force. In this study, we use the combined stiffness and viscous form of the Flanagan–Belytschko hourglass control, see [27, 28] for details.

As shown in Equations (40)–(43), when we compute the force vectors for a cracked element, we only modify them by the volume fraction. Such modification can be easily embedded into the standard element process of the finite element method. This is a remarkable merit of the phantom node method in comparison with the conventional XFEM.

6. NUMERICAL EXAMPLES

6.1. Edge-cracked plate under impulsive loading

Kalthoff and Winkler [37] reported an experiment in which a plate with two edge notches is impacted by a projectile as shown in Figure 6. The experiment showed two different failure modes with different projectile speeds: at high impact velocities, a shear band was observed to propagate from the tip of the notch at a negative angle of about $-10°$; at lower impact velocities, a brittle fracture mode with a propagation angle of about $70°$ was observed. Two-dimensional analysis of this example was carried out by Belytschko *et al.* [11, 38, 39] for the brittle fracture mode and Song *et al.* [13] for both modes. In this study, we only consider the brittle failure mode.

Owing to the symmetry, only the upper half of the plate is simulated. The boundary conditions are: on the bottom edge of the model, the symmetry condition is applied, i.e. $\bar{u}_y = 0$ and $\bar{t}_x = 0$; on the left edge for $0 \leqslant y \leqslant 25$ mm, a velocity $v_0 = 16.5$ m/s is applied; the other edges are traction-free. For this impulse, a brittle failure mode was observed in the experiment. The initial notch is simulated by a discontinuity represented by XFEM [8]. The material properties are $E = 190$ GPa, $v = 0.3$, $\rho = 8000$ kg/m^3 and fracture energy $G_f = 2.217 \times 10^4$ J/m^2. The tensile strength is $\sigma_f = 844$ MPa which corresponds to a fracture strain $\varepsilon_f = 0.0044$. The Courant number for the time integration is 0.2.
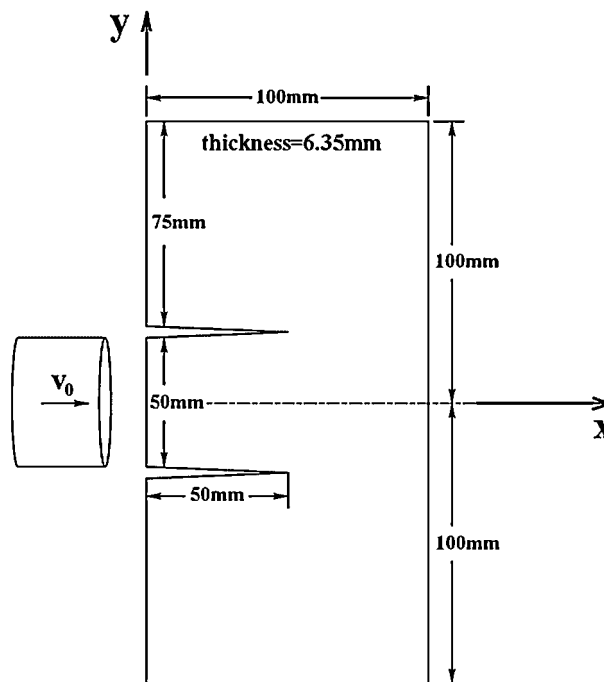
Figure 6. Experimental set-up for edge-cracked plate under impulsive loading reported by Kalthoff and Winkler [37].
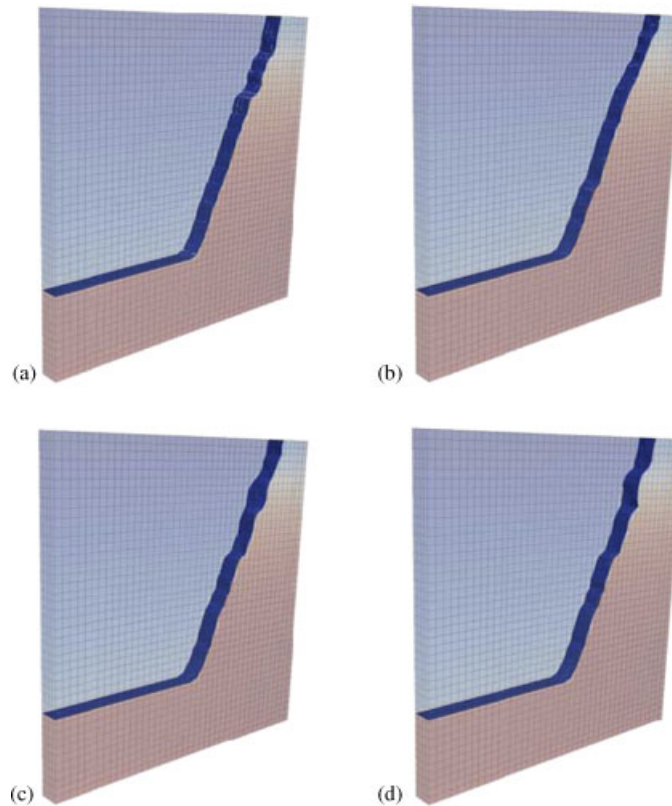
Figure 7. Comparison of final crack surface with different weights by using coarse mesh: (a) $w=0.1$,
$\eta^a=3.71\%$; (b) $w=1, \eta^a=11.55\%$; (c) $w=10, \eta^a=16.26\%$; and (d) $w=100, \eta^a=17.16\%$.

We studied this problem with three uniform meshes: $42\times42\times4$, $62\times62\times6$ and $82\times82\times8$. The typical element size h of the three meshes are, respectively, $h=2.38$, 1.61 and 1.22 mm. Figure 7 shows the crack surfaces of the coarse mesh with four different weights for w_I in Equation (15): $w_I=0.1, 1, 10, 100$. The resulting crack surfaces are similar. However, the larger the weight, the bigger the error in the fracture directionality η^a defined by

$$\eta^a = \frac{1}{n_c} \sum_{e=1}^{n_c} \frac{\int_{\Omega_0^e} \|\mathbf{N}^e - \mathbf{n}(f_I^e)\| \, d\Omega_0^e}{\Omega_0^e} \tag{46}$$

where n_c is the number of cracked elements. However, small weights lead to discontinuities in the crack surfaces as shown in Figure 8. To take both the continuity and the fracture directionality into consideration, $w=1$ is employed in subsequent simulations.

The crack paths for different meshes are shown in Figures 9 and 10. The two meshes give similar crack paths, i.e. mesh dependence in terms of the shape of the crack surface is not observed. The crack surfaces are nearly normal to the planes of the plate. The overall crack propagation angle is about $66°$ which agrees reasonably well with the experimental value of about $70°$ and with the previous two-dimensional results [11, 13].
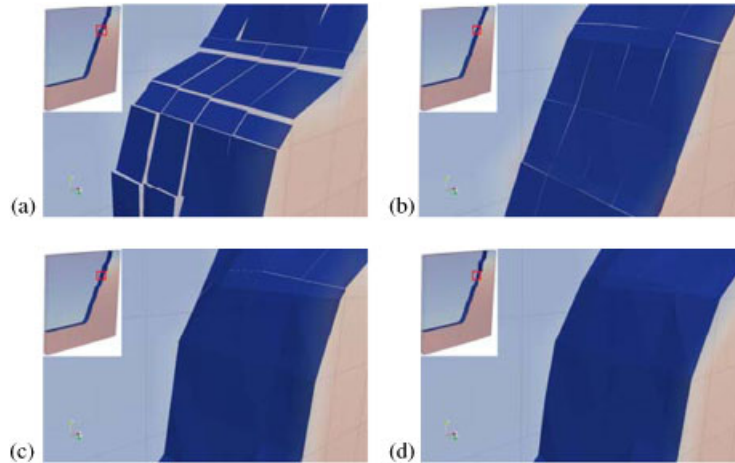
Figure 8. Close-up view of the crack surface generated by different weights:
(a) $w=0.1$; (b) $w=1$; (c) $w=10$; and (d) $w=100$.

The evolution of the crack length is plotted in Figure 11, where the crack length $l(t)$ is defined by

$$l(t) = \frac{A(t)}{\kappa} \tag{47}$$

where $A(t)$ is the area of the crack surface and κ is the thickness of the specimen. It is observed that the three meshes give similar results, i.e. the crack starts to propagate at about 25 μs and the propagation speed is almost constant. The crack velocity averages about 1730 m/s which agrees well with the result from the two-dimensional analysis [11] where it was 1800 m/s. However, we observed some mesh dependence: the denser the mesh, the earlier the crack will start to propagate and the higher the velocity. This mesh dependence probably arises because the finer mesh can capture the high-gradient strain field ahead of the crack front more accurately than the coarse mesh.

Time histories of the cohesive fracture energy for different mesh refinements are shown in Figure 12. It is observed that after the crack starts to propagate, the release rate of the cohesive fracture energy remains nearly constant during the period of propagation. Again, a little mesh dependence is present, i.e. the denser the mesh, the earlier the cohesive fracture energy will be dissipated with a higher release rate.

6.2. Pull-out test

This example models the pull-out of a steel anchor embedded in a concrete cylindrical block 1400 mm in diameter and 600 mm in thickness. Areias and Belytschko [20] and Gasser and Holzapfel [21] simulated the same problem by quasi-static analysis. Here we model this problem by dynamic analysis to demonstrate our method for non-planar cracking problems.

Geometrical data are shown in Figure 13. Owing to four-fold symmetry, just one quarter of the concrete block is simulated and the symmetry conditions are applied on the surfaces $x=0$ and $y=0$, respectively. The velocity of the dark area in Figure 13 on the top of the block is fixed in the z direction. The effect of the steel anchor is represented by imposing a vertical velocity on the
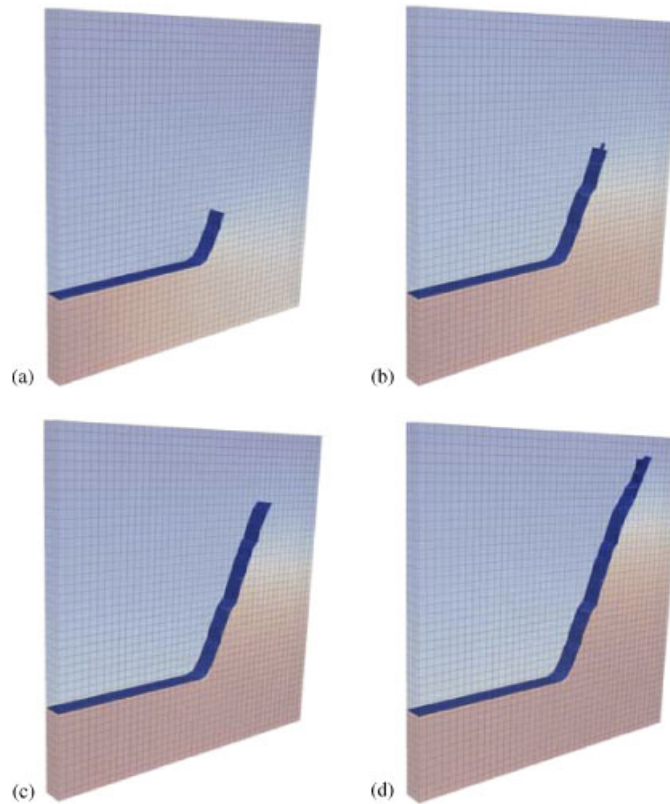
Figure 9. Propagation of crack surface by using coarse mesh ($h=2.38\,$mm): (a) $t=40.02\,\mu$s; (b) $t=54.44\,\mu$s; (c) $t=67.61\,\mu$s; and (d) $t=82.33\,\mu$s.

bottom surface where the block interacts with the anchor stem (shaded area in Figure 13). The prescribed vertical velocity is increased linearly to 0.01 m/s in 5 ms and then hold constant.

The material properties are $E=30\,$GPa, $v=0.2$, $\rho=2400\,$kg/m^3 and fracture energy $G_f = 1.06\times10^2\,$J/m^2. The tensile fracture stress is set as $\sigma_f=3\,$MPa which corresponds to a fracture strain $\varepsilon_f=0.0001$. Three meshes are used in simulation which consist of 9904, 30 180 and 61 792 hexahedral elements, respectively. The typical element size h of the three meshes is, respectively, $h=35.0$, 23.3 and 17.5 mm.

Figures 14 and 15 show the crack surface of the coarse mesh with four different weights. Again, $w=1$ is a good choice to balance the continuity of the crack surface and the fracture directionality. Only this value is used in the following results.

Figures 16–18 show the crack surface resulted by the three meshes, respectively. The crack starts from the bottom interface of the block and propagates to the upper edge. The final surface forms a cone. The shapes of the crack surfaces computed by the three meshes are similar and agree well with the quasi-static results [20, 21].

The evolution of the dissipated cohesive energy is shown in Figure 19. The crack is generated and starts to propagate at around 10 ms. The propagation is accelerated at around 25 ms (which
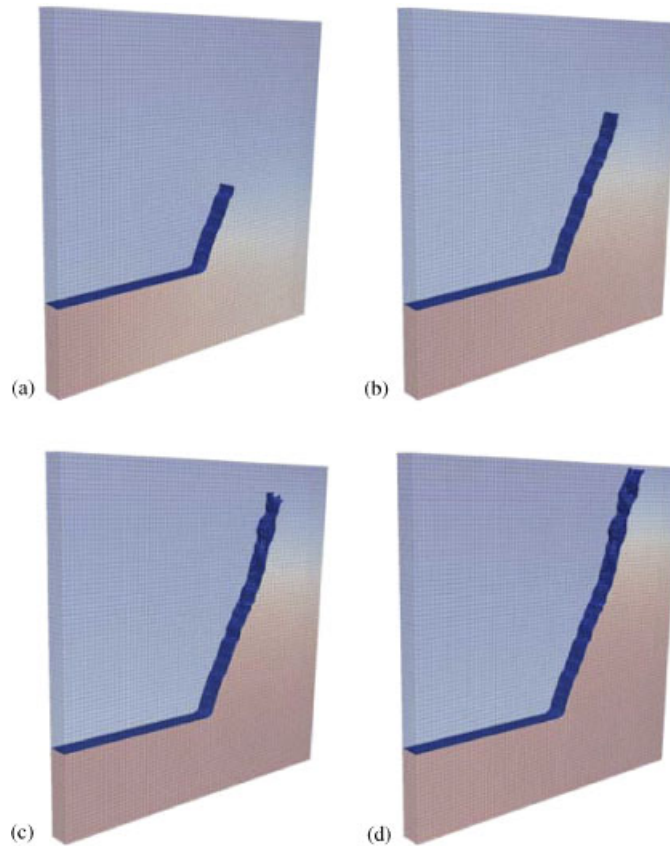
Figure 10. Propagation of crack surface by using refined mesh ($h = 1.22$ mm):
(a) $t = 40.11$ μs; (b) $t = 53.76$ μs; (c) $t = 68.26$ μs; and (d) $t = 82.28$ μs.

corresponds to a loading displacement of about 0.23 mm) and the dissipated cohesive energy increases rapidly. This phenomenon is also observed by Gasser and Holzapfel [21]. The crack growth slows at around $t = 35$ ms and almost stops at around $t = 38$ ms. The final dissipated cohesive energies of the three meshes are almost identical.

   Figure 20 shows the load–displacement response. The material constitutive models in this study and Gasser and Holzapfel [21] are only elastic, while Areias and Belytschko [20] considered damage and plastic effects. Initially, our results coincide with the quasi-static results of Gasser and Holzapfel [21] and are oscillation-free. However, when the crack is initiated at a displacement of 0.075 mm (which corresponds to $t = 10$ ms in Figure 19), our results starts to oscillate. At a displacement of 0.23 mm (which corresponds to $t = 25$ ms in Figure 19), the load suddenly drops due to the accelerated crack propagation which also causes the rapid increase of the dissipated cohesive energy shown in Figure 19. After the accelerated cracking process is finished, the load is re-increased slowly at displacement of 0.32 mm which corresponds to $t = 35$ ms in Figure 19. The phenomena of the re-increase of the load is also presented in the result of Gasser and Holzapfel [21] while it is not observed by Areias and Belytschko [20], which is maybe caused by the effect
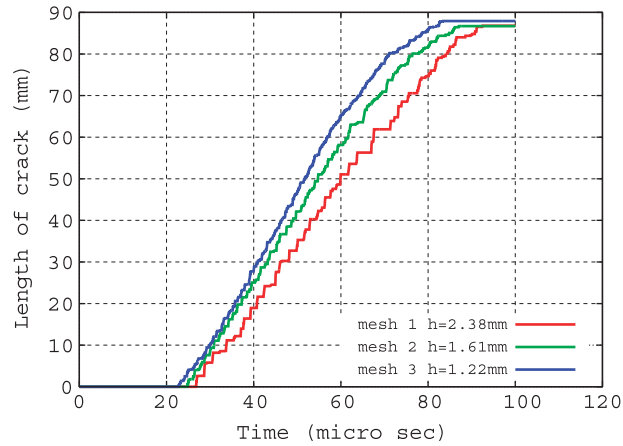
Figure 11. Evolution of crack length of the edge-cracked plate under impulsive loading problem.
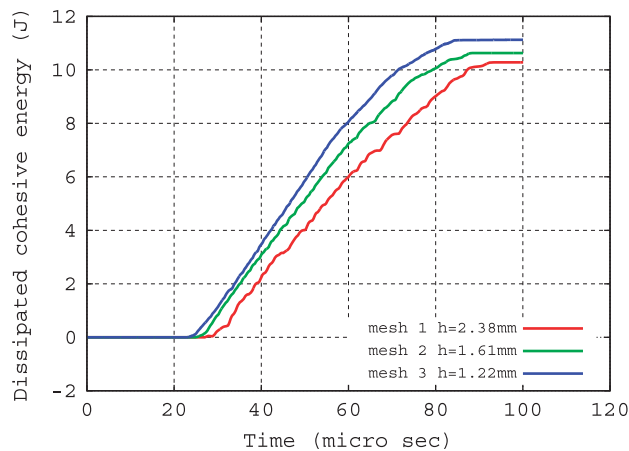

Figure 12. Time histories of the cohesive fracture energy for the edge-cracked plate
under impulsive loading problem.

of damage. The shape of the curves and thus the whole load–displacement response of both the elastic results, i.e. Gasser and Holzapfel [21] and the present study, are qualitatively similar.

Figure 21 shows the final deformed configuration of the concrete block where the displacement is magnified by a factor of 500. The shape is consistent to the result given in paper [21].

7. CONCLUSIONS

An approximate level set method for three-dimensional crack propagation has been presented. In this method, the level sets for representing the crack surface are localized to each cracked element.
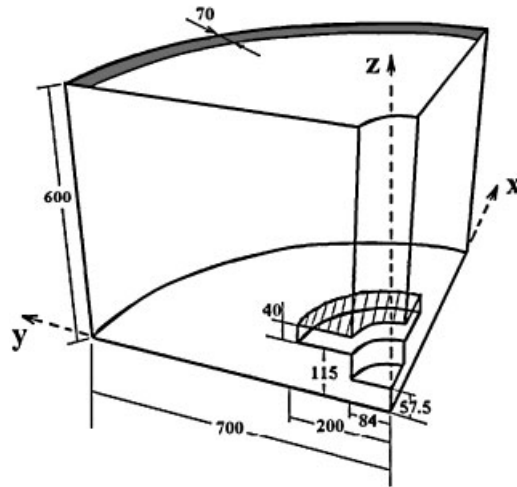
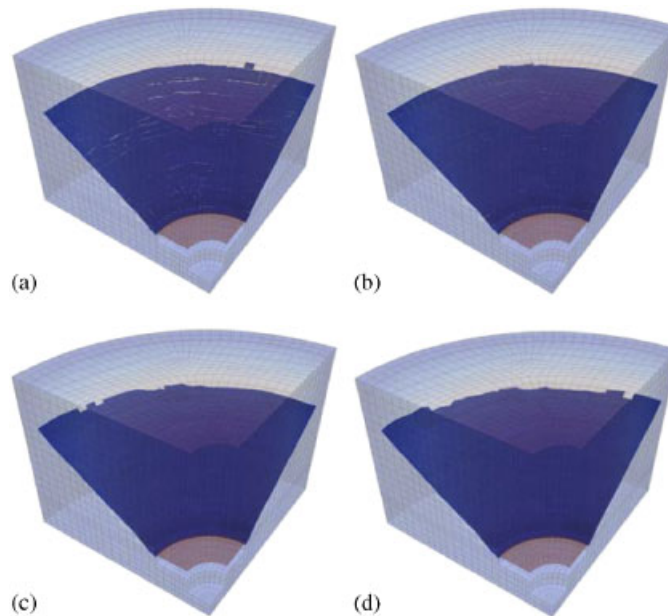Figure 13. Geometry of the anchorage structure (unit in millimeter).

Figure 14. Comparison of final crack surface with different weights by using coarse mesh: (a) $w=0.1, \eta^a=2.43\%$; (b) $w=1, \eta^a=6.08\%$; (c) $w=10, \eta^a=8.09\%$; and (d) $w=100, \eta^a=8.78\%$.

We call this an element-local level set (ELLS) method. When the crack propagates, the ELLSs are generated for the newly cracked elements by a procedure that meets fracture directionality and continuity of the crack in a least-square sense. In contrast with the conventional level set method, it does not require the velocity of the crack front to update the level sets. This is quite
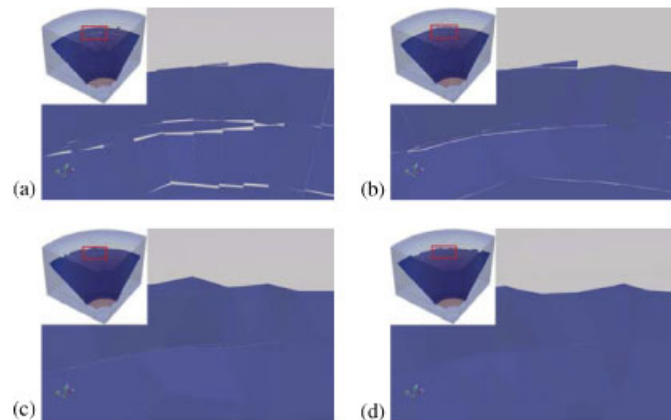
Figure 15. Close-up view of the crack surface generated by different weights: (a) $w=0.1$;
(b) $w=1$; (c) $w=10$; and (d) $w=100$.
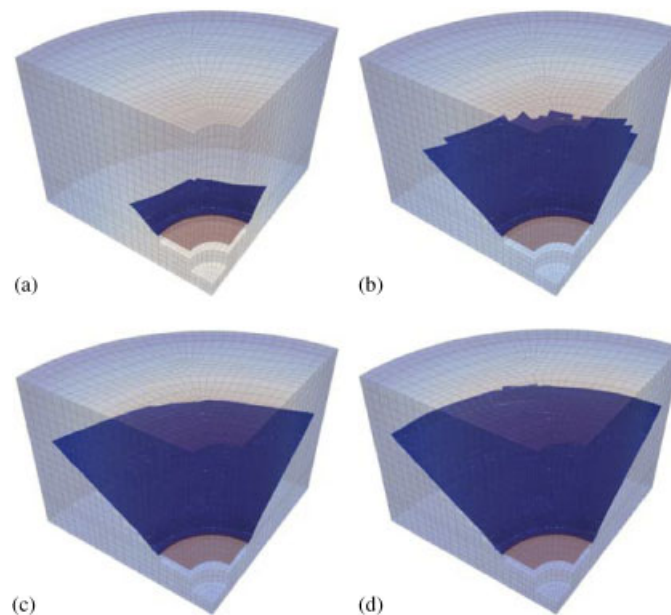

Figure 16. Propagation of crack surface by using mesh 1 with typical element size $h=35.0$ mm:
(a) $t=19.32$ ms; (b) $t=26.99$ ms; (c) $t=33.13$ ms; and (d) $t=42.50$ ms.

important, because many fracture criteria, such as phenomenological criteria, criteria based on
material instability or maximum principal strain do not provide a velocity of the crack front.
The proposed method can easily deal with these types of fracture criteria. Furthermore, unlike in
conventional level set methods, the update does not require the solution of global partial differential
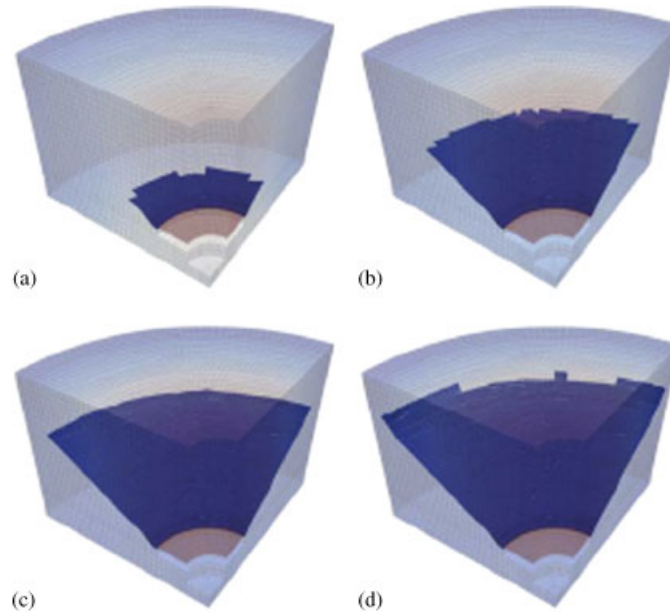equations; hence, it is quite simple and efficient.

Figure 17. Propagation of crack surface by using mesh 2 with typical element size $h=23.3$ mm: (a) $t=19.20$ ms; (b) $t=27.06$ ms; (c) $t=32.66$ ms; and (d) $t=42.50$ ms.
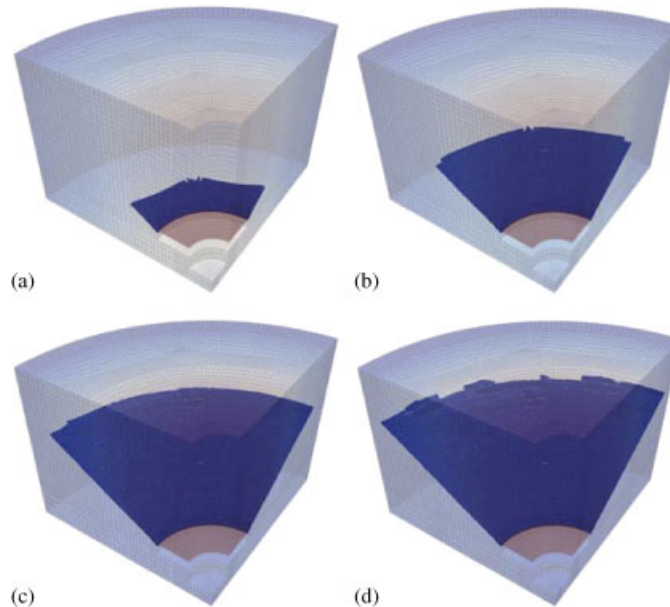

Figure 18. Propagation of crack surface by using mesh 3 with typical element size $h=17.5$ mm: (a) $t=19.07$ ms; (b) $t=26.98$ ms; (c) $t=32.85$ ms; and (d) $t=42.50$ ms.
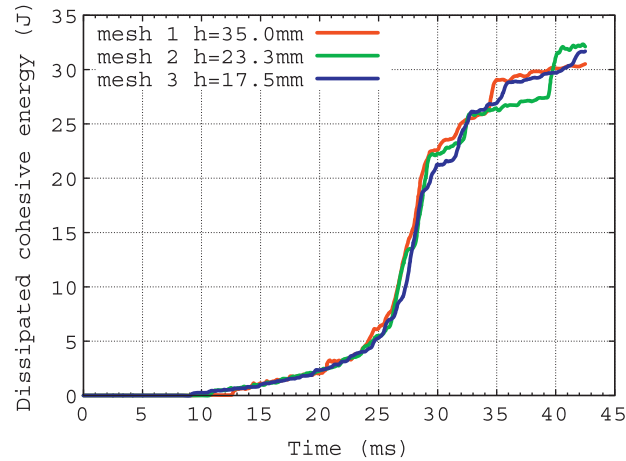
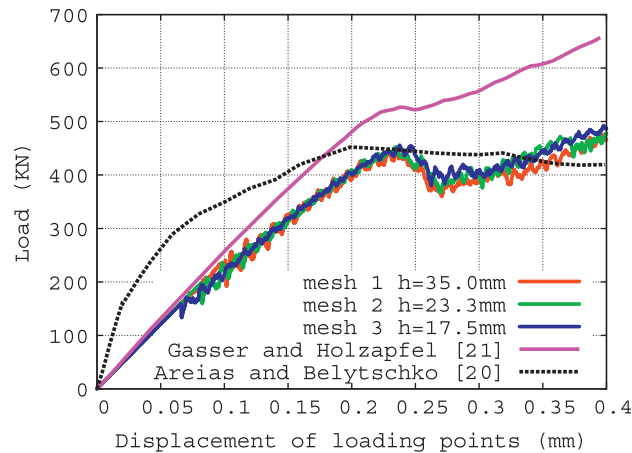Figure 19. Energy dissipated by cohesive force.

Figure 20. Load versus displacement of loading points.

The ELLS method has been combined with the phantom node method, which has been extended to three dimensions; the latter is based on the paradigm for discontinuities proposed by Hansbo and Hansbo [15] but the basis function are identical to those of XFEM. The ability of the combined method for modeling three-dimensional planar and non-planar dynamic crack propagation has been demonstrated by two examples: the edge-cracked plate under impulsive loading and the pull-out test. In both cases, our results agree well with the available experimental or numerical results in the literature. We did not observe mesh dependence in terms of the shape of the crack surface. However, some mesh dependence of start time and the velocity of the crack propagation was observed. This mesh dependence was probably due to the improved accuracy of the finer meshes in computing strains and the consequent effects on the maximum principal strain fracture criterion.
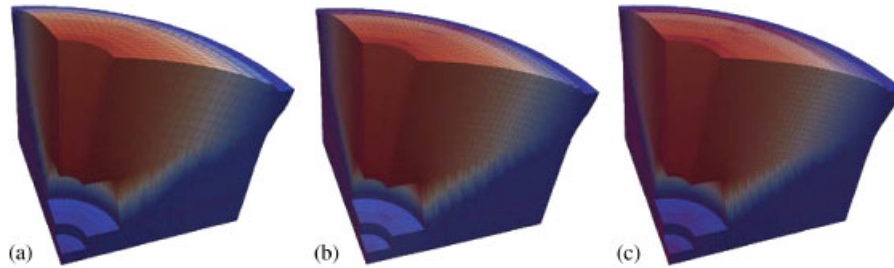
Figure 21. Final deformed body of the anchorage structure (displacement magnified by a factor of 500): (a) mesh 1, $h = 35.0$ mm; (b) mesh 2, $h = 23.3$ mm; and (c) mesh 3, $h = 17.5$ mm.

Though the method was described in the context of 8-node hexahedra, it is applicable to a variety of low-order elements, such as tetrahedra and pentahedra. The general concept of extending crack surfaces by methods that respect continuity and crack direction in a least-square sense may also be applicable to higher-order elements.

The two examples we investigated in this study both contained only one continuous crack surface. However, these ELLS methods can be extended to describe multiple crack surfaces to simulate problems such as three-dimensional fragmentation. These aspects will be further studied in the future.

ACKNOWLEDGEMENTS

REFERENCES

1. Belytschko T, Fish J, Engelmann BE. A finite element with embedded localization zones. *Computer Methods in Applied Mechanics and Engineering* 1988; **70**:59–89.
2. Simo JC, Oliver J, Armero F. An analysis of strong discontinuities induced by strain-softening in rate-independent inelastic solids. *Computational Mechanics* 1993; **12**(5):277–296.
3. Dvorkin EN, Cuitino AM, Gioia G. Finite elements with displacement interpolated embedded localization lines insensitive to mesh size and distortions. *International Journal for Numerical Methods in Engineering* 1990; **30**(3):541–564.
4. Jirásek M. Comparative study on finite elements with embedded discontinuities. *Computer Methods in Applied Mechanics and Engineering* 2000; **188**(1–3):307–330.
5. Xu XP, Needleman A. Numerical simulations of fast crack growth in brittle solids. *Journal of the Mechanics and Physics of Solids* 1994; **42**:1397–1434.
6. Ortiz M, Pandolfi A. Finite-deformation irreversible cohesive elements for three-dimensional crack-propagation analysis. *International Journal for Numerical Methods in Engineering* 1999; **44**(9):1267–1282.
7. Belytschko T, Black T. Elastic crack growth in finite elements with minimal remeshing. *International Journal for Numerical Methods in Engineering* 1999; **45**:601–620.
8. Moës N, Dolbow J, Belytschko T. A finite element method for crack growth without remeshing. *International Journal for Numerical Methods in Engineering* 1999; **46**(1):131–150.
9. Dolbow J, Moës N, Belytschko T. Discontinuous enrichment in finite elements with a partition of unity method. *Finite Elements in Analysis and Design* 2000; **36**(3):235–260.
10. Belytschko T, Moës N, Usui S, Parimi C. Arbitrary discontinuities in finite elements. *International Journal for Numerical Methods in Engineering* 2001; **50**(4):993–1013.

11. Belytschko T, Chen H, Xu J, Zi G. Dynamic crack propagation based on loss of hyperbolicity and a new discontinuous enrichment. *International Journal for Numerical Methods in Engineering* 2003; **58**:1873–1905.
12. Réthoré J, Gravouil A, Combescure A. An energy-conserving scheme for dynamic crack growth using the extended finite element method. *International Journal for Numerical Methods in Engineering* 2005; **63**:631–659.
13. Song JH, Areias PMA, Belytschko T. A method for dynamic crack and shear band propagation with phantom nodes. *International Journal for Numerical Methods in Engineering* 2006; **67**:868–893.
14. Menouillard T, Réthoré J, Moës N, Combescure A, Bung H. Mass lumping strategies for X-FEM explicit dynamics: application to crack propagation. *International Journal for Numerical Methods in Engineering* 2008; **74**:447–474.
15. Hansbo A, Hansbo P. A finite element method for the simulation of strong and weak discontinuities in solid mechanics. *Computer Methods in Applied Mechanics and Engineering* 2004; **193**(33–35):3523–3540.
16. Osher S, Sethian JA. Fronts propagating with curvature-dependent speed: algorithms based on Hamilton–Jacobi formulations. *Journal of Computational Physics* 1988; **79**:12–49.
17. Stolarska M, Chopp DL, Moës N, Belytschko T. Modelling crack growth by level sets in the extended finite element method. *International Journal for Numerical Methods in Engineering* 2001; **51**:943–960.
18. Moës N, Gravouil A, Belytschko T. Non-planar 3D crack growth by the extended finite element and level sets. Part I : mechanical model. *International Journal for Numerical Methods in Engineering* 2002; **53**(11): 2549–2568.
19. Gravouil A, Moës N, Belytschko T. Non-planar 3D crack growth by the extended finite element and level sets. Part II: level set update. *International Journal for Numerical Methods in Engineering* 2002; **53**:2569–2586.
20. Areias PMA, Belytschko T. Analysis of three-dimensional crack initiation and propagation using the extended finite element method. *International Journal for Numerical Methods in Engineering* 2005; **63**:760–788.
21. Gasser TC, Holzapfel GA. Modeling 3D crack propagation in unreinforced concrete using PUFEM. *Computer Methods in Applied Mechanics and Engineering* 2005; **194**(25–26):2859–2896.
22. Gasser TC, Holzapfel GA. 3D Crack propagation in unreinforced concrete. A two-step algorithm for tracking 3D crack paths. *Computer Methods in Applied Mechanics and Engineering* 2006; **195**(37–40):5198–5219.
23. Jäger P, Steinmann P, Kuhl E. Modeling three-dimensional crack propagation—a comparison of crack path tracking strategies. *International Journal for Numerical Methods in Engineering* 2008; **76**:1328–1352.
24. Pereira JP, Duarte CA, Guoy D, Jiao X. hp-generalized FEM and crack surface representation for non-planar 3-D cracks. *International Journal for Numerical Methods in Engineering* 2009; **77**(5):601–633.
25. Duarte CA, Hamzeh ON, Liszka TJ, Tworzydlo WW. A generalized finite element method for the simulation of three-dimensional dynamic crack propagation. *Computer Methods in Applied Mechanics and Engineering* 2001; **190**(15–17):2227–2262.
26. Duarte CA, Reno LG, Simone A. High-order generalized FEM for through-the-thickness branched cracks. *International Journal for Numerical Methods in Engineering* 2007; **72**:325–351.
27. Flanagan DP, Belytschko T. A uniform strain hexahedron and quadrilaterals with high coarse-mesh accuracy. *International Journal for Numerical Methods in Engineering* 1981; **17**:679–706.
28. Daniel WJT, Belytschko T. Suppression of spurious intermediate frequency modes in under-integrated elements by combined stiffness/viscous stabilization. *International Journal for Numerical Methods in Engineering* 2005; **64**:335–353.
29. Barenblatt GI. The mathematical theory of equilibrium cracks formed in brittle fracture. *Advances in Applied Fracture* 1962; **7**:55–129.
30. Dugdale DS. Yielding of steel sheets containing slits. *Journal of the Mechanics and Physics of Solids* 1960; **8**(2):100–104.
31. Hillerborg A, Modeer M, Petersson PE. Analysis of crack formation and crack growth in concrete by means of fracture mechanics and finite elements. *Cement and Concrete Research* 1976; **6**(6):773–782.
32. Planas J, Elices M. Nonlinear fracture of cohesive materials. *International Journal of Fracture* 1991; **51**(2): 139–157.
33. Rabczuk T, Song JH, Belytschko T. Simulations of instability in dynamic fracture by the cracking particles method. *Engineering Fracture Mechanics*, in early view. DOI: 10.1016/j.engfracmech.2008.06.002.
34. Song JH, Wang HW, Belytschko T. A comparative study on finite element methods for dynamic fracture. *Computational Mechanics* 2008; **42**(2):239–250.
35. Papoulia KD, Sam CH, Vavasis SA. Time continuity in cohesive finite element modeling. *International Journal for Numerical Methods in Engineering* 2003; **58**:679–701.
36. Belytschko T, Liu WK, Moran B. *Nonlinear Finite Elements for Continua and Structures*. Wiley: New York, 2000.

37. Kalthoff JF, Winkler S. Failure mode transition at high rates of shear loading. *Proceedings of the International Conference on Impact Loading and Dynamic Behavior of Materials* 1988; **1**:185–195.
38. Belytschko T, Lu YY, Gu L, Tabbara M. Element-free Galerkin methods for static and dynamic fracture. *International Journal of Solids and Structures* 1995; **32**(17–18):2547–2570.
39. Belytschko T, Tabbara M. Dynamic fracture using element-free Galerkin methods. *International Journal for Numerical Methods in Engineering* 1996; **39**:923–938.